applied sciences

MDPI

Article

Study on Suppression Strategy for Broadband Sub-Synchronous Oscillation in Doubly-Fed Wind Power Generation System

Dongyang Sun *, Fanyi Meng and Wenqiang Shen

Engineering Research Center of Automotive Electronics Drive Control and System Integration, Ministry of Education, Harbin University of Science and Technology, Harbin 150080, China
* Correspondence: ggdaxx@163.com

Abstract: In the power transmission of doubly-fed induction generators (DFIGs), sub-synchronous oscillation (SSO) can occur due to the influence of series compensation capacitance and long-distance transmission. SSO not only affects the output of the DFIG but also leads to oscillation diffusion. In order to solve the problem of disturbance in the control of the DFIG rotor side converter (RSC) under SSO, an adaptive quasi-resonant controller is proposed for the suppression of SSO. This strategy focuses on the propagation path of and frequency change in the SSO in the RSC control system and suppresses the SSO current in the wideband through the cooperative control of the back-stepping controller and the adaptive quasi-resonant controller. In this way, the stator-side output of the DFIG will not be affected by SSO, thus avoiding the amplification of the sub-synchronous power of the line by the DFIG. A simulation model and experimental platform were built to verify the suppression effect of this control strategy on the DFIG stator sub-synchronous current at different SSO frequencies. The results show that the proposed strategy has a good suppression effect on broadband SSO.

Keywords: doubly-fed induction generator; frequency of the sub-synchronous oscillation changes; rotor side converter; DFIG decoupling model; back-stepping controller; adaptive quasi-resonant controller

check for updates

Citation: Sun, D.; Meng, F.; Shen, W. Study on Suppression Strategy for Broadband Sub-Synchronous Oscillation in Doubly-Fed Wind Power Generation System. *Appl. Sci.* **2022**, *12*, 8344. https://doi.org/10.3390/app12168344

Academic Editor: Gilsoo Jang

Received: 5 July 2022
Accepted: 18 August 2022
Published: 20 August 2022

Publisher's Note: MDPI stays neutral with regard to jurisdictional claims in published maps and institutional affiliations.

Copyright: © 2022 by the authors. Licensee MDPI, Basel, Switzerland. This article is an open access article distributed under the terms and conditions of the Creative Commons Attribution (CC BY) license (https://creativecommons.org/licenses/by/4.0/).

1. Introduction

With the development of modern power systems, the proportion of wind energy and other new energies in power systems is increasing. Doubly-fed induction generators (DFIGs), as the most commonly used wind turbine type, often need to transmit over long distances during power transmission [1]. In the process of long-distance power transmission, in order to reduce the energy loss in the line and improve the transmission efficiency, a scheme for connecting compensation capacitors in series in the transmission line is often adopted [2]. However, due to the fact that the DFIG converter contains a large number of power electronic components, the interaction between the converters and the series compensation capacitors may cause sub-synchronous oscillations (SSO) in the wind power system [3,4]. Mild SSOs can cause the output power of wind-driven generators to oscillate, which can affect the lower line; if it is serious, it can cause the wind-driven generator to be disconnected from the grid, and the thermal power and other generator sets will be cut off [5–7]. In 2009, the power system of the US state of Texas experienced high line series compensation, causing sub-synchronous oscillation resulting in wind generator failures [8]. Since 2012, due to the high degree of series compensation in transmission lines, a number of synchronous oscillation accidents have occurred in doubly-fed wind farms in Guyuan district, Hebei Province, China, resulting in the waste of wind energy and the off-gridding of a large number of wind turbines [9]. Therefore, research on the suppression of SSO in DFIG grid-connected systems has important significance.

In order to suppress the accidents caused by the SSO of DFIG grid-connected systems, scholars from various countries have proposed many methods. Among them, adding

an SSO damper and improving the control strategy for the converter are the most common [10,11]. Shair introduced an SSO damper on the dq axis of the RSC current control to alleviate the influence of SSO by improving the damping of the RSC control system [12]. Leon proposed to add a double-damping compensation filter to the RSC to improve the system damping and increase the flexibility of the control system, reducing the oscillation and overshoot of the rotor voltage and thereby mitigating the SSO phenomenon in DFIG wind farms [13]. The abovementioned suppression measures involving addition of dampers are relatively traditional, and the difficulty of implementation is low. However, the applicability of these strategies is not strong, and the suppression effect on the SSO is not flexible enough; furthermore, they can generally only eliminate oscillations at specific frequencies. Improving the converter control strategy is also a common way of suppressing SSOs in DFIG systems. Zhang et al. designed a notch filter on the power feedback branch and current feedback branch of an RSC in accordance with the impedance scanning method [14]. This scheme has excellent inhibitory effects on low-frequency oscillations but no obvious inhibitory effects on oscillations at 15 Hz and above. Meng et al. utilized a quasi-resonant controller's static-free adjustment capability for AC signals. The quasi-resonant controller was used on the rotor side to suppress the stator sub-synchronous current and also on the grid side to suppress the sub-synchronous oscillation of the DC side voltage and reactive power, but the case of SSO frequency variation was not considered [15].

Aiming at the SSO problem in DFIG systems, this paper proposes an RSC back-stepping SSO suppression strategy based on an adaptive quasi-resonant controller. First, the mechanism of SSO generation was analyzed and the mathematical model for the RSC under the SSO state was established. By analyzing the process of the interference of grid SSO on RSC control, it was determined that there are three propagation paths for the SSO in the RSC control system, and the influence of SSO frequency changes on the generator stator current was also analyzed. Drawing on the Lyapunov stability theorem, an RSC current back-stepping controller based on the DFIG decoupling model was designed to replace the traditional PI controller that made it possible simplify the control of the RSC and reduce the SSO input into the RSC system path. At the same time, in order to suppress the variable frequency SSO, an adaptive quasi-resonant controller was designed to track the stator current in the SSO state, and its output was input to the RSC control system as a compensation amount to compensate the output voltage command of the RSC controller, finally eliminating the SSO component in the stator current and achieving a stable output state. Through simulation and experimental verification, the proposed back-stepping SSO suppression strategy based on an adaptive quasi-resonant controller was found to be able to stabilize the generator stator current output at different SSO frequencies and had a good suppression effect on the SSO of the DFIG system.

2. Analysis of Influence of SSO on DFIG System Operation

2.1. The Establishment of the Mathematical Model for an RSC with SSO

The DFIG control model adopted in this study is shown in Figure 1. This double-closed-loop vector control (VC) model is one of the most widely used DFIG control models. The VC control model has the advantages of utilizing mature regulation technology and showing good steady-state performance and strong robustness [16]. The grid-side converter in the figure is represented by the term "GSC", while the SSO component of the power grid is marked with red arrows.

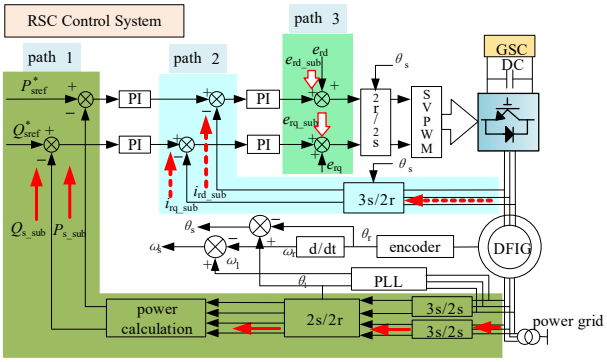

Figure 1. Schematic diagram of SSO propagation in RSC control system.

As can be seen from Figure 1, the SSO is input into the RSC control system through three paths successively. These three paths are the power outer loop, the current inner loop and the feedforward decoupling compensation. All oscillations are indicated by the subscript "sub", and "*" represents the reference value for the input signal.

Utilizing the voltage equation, the flux linkage equation and the power calculation for the DFIG system, the mathematical model for the RSC current control under SSO can be obtained through coordinate transformation [17,18]:

$$\begin{cases} u_{\mathrm{rd}} = R_{\mathrm{r}}\widetilde{i}_{\mathrm{rd}} + \sigma L_{\mathrm{r}}\frac{\mathrm{d}\widetilde{i}_{\mathrm{rd}}}{\mathrm{d}t} - \omega_{\mathrm{s}}[-\frac{L_{\mathrm{m}}}{\omega_1 L_{\mathrm{s}}}U_{\mathrm{s}} + \sigma L_{\mathrm{r}}\widetilde{i}_{\mathrm{rd}}] \\ u_{\mathrm{rq}} = R_{\mathrm{r}}\widetilde{i}_{\mathrm{rq}} + \sigma L_{\mathrm{r}}\frac{\mathrm{d}\widetilde{i}_{\mathrm{rq}}}{\mathrm{d}t} + \omega_{\mathrm{s}}\sigma L_{\mathrm{r}}\widetilde{i}_{\mathrm{rq}} \end{cases} \tag{1}$$

In Equation (1), u_{rd} and u_{rq} are the d and q components of the rotor voltage, respectively; R_{r} is the rotor winding resistance; $\widetilde{i}_{\mathrm{rd}}$ and $\widetilde{i}_{\mathrm{rq}}$ are the d and q components of the rotor current; L_{s} is the self-inductance of the stator winding; L_{r} is the rotor winding self-inductance; L_{m} is the mutual inductance between the equivalent windings of the stator and rotor; $\sigma = 1 - L_{\mathrm{m}}^2/L_{\mathrm{s}}L_{\mathrm{r}}$ is the leakage flux coefficient of the motor; ω_{s} is the slip angle frequency, and $\omega_{\mathrm{s}} = \omega_1 - \omega_{\mathrm{r}}$; ω_1 is the synchronization angular frequency; and ω_{r} is the rotor angular frequency.

According to Figure 1, when the grid produces SSO, the sub-synchronous current in the grid is fed into the stator side of the DFIG. Through the electromagnetic induction effect, the stator sub-synchronous current induces the corresponding sub-synchronous current on the generator rotor side. At the same time, the oscillation of the stator current also causes the DFIG power oscillation, resulting in an RSC power outer-ring output instruction oscillation. The waveform distortion and phase shift of the stator and rotor side currents make the oscillating components affect the RSC control circuit, causing the control command signal generated by the RSC to oscillate, which further affects the actual current in the rotor and causes the DFIG output power to oscillate.

In conclusion, when the grid SSO is generated, since the RSC control is disturbed by the oscillation in the stator current, the DFIG stator current produces the corresponding sub-synchronous component. The stator three-phase sub-synchronous current generated by the DFIG is calculated as follows:

$$\begin{cases} \Delta i_{\mathrm{sa\_sub}} = \sqrt{2}|h|I_{\mathrm{n}}\cos(\omega_{\mathrm{n}}t + \phi_{\mathrm{in}} + \pi - \phi) \\ \Delta i_{\mathrm{sb\_sub}} = \sqrt{2}|h|I_{\mathrm{n}}\cos(\omega_{\mathrm{n}}t + \phi_{\mathrm{in}} + 5\pi/3 - \phi) \\ \Delta i_{\mathrm{sc\_sub}} = \sqrt{2}|h|I_{\mathrm{n}}\cos(\omega_{\mathrm{n}}t + \phi_{\mathrm{in}} + \pi/3 - \phi) \end{cases} \tag{2}$$

In Equation (2), ϕ represents the phase difference between the sub-synchronous current component generated by the RSC control and the sub-synchronous current component in the original stator and h is the amplitude amplification ratio between the two; I_{n} is the RMS value of the original stator sub-synchronous current component; ω_{n} is the angle

frequency of the grid sub-synchronous oscillation; and φ_{in} is the initial phase angle of the stator sub-synchronous current in the d-q coordinate system.

Superimposing the sub-synchronous current output from the DFIG results in its superimposition with the original sub-synchronous current in the stator. When they satisfy a certain phase relation, the amplitude of the sub-synchronous current with frequency ω_n is increased. At this time, the line with higher series compensation in the power grid interacts with the RSC, and a positive feedback link is formed between them to generate the sub-synchronous current of the stator, resulting in the divergence of oscillation.

2.2. Analysis of Influence of SSO Frequency Variation on DFIG System

By analyzing the mathematical model of the RSC under SSO, we can understand the divergence process in the sub-synchronous current in the DFIG system. However, the establishment of the corresponding mathematical model in Section 2.1 was based on the assumption that the oscillation frequency within the input DFIG system is a fixed value. The change in the oscillation frequency may have an impact on the output of the DFIG system and the control effect of the SSO suppression strategy. In order to verify the influence of the SSO frequency variation on the designed oscillation suppression strategy for the DFIG system, as done in [15], simulation and analysis of an SSO suppression strategy for a DFIG system based on a quasi-resonant controller were carried out.

Firstly, the output of the DFIG with the grid SSO was observed, and the simulation results are shown in Figure 2.

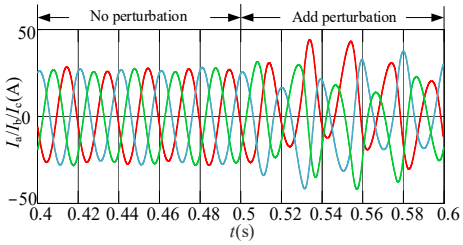

Figure 2. The stator current waveform output by the DFIG.

Figure 2 shows a comparison of the DFIG output stator current waves before and after the generation of the power grid SSO. The simulated condition was that, at 0.5 s, the grid frequency was 10 Hz and the oscillation amplitude was 20% of the grid base wave voltage. It can be seen from Figure 2 that the DFIG output stator current was a three-phase sinusoidal alternating current before 0.5 s. After 0.5 s, due to the influence of the SSO of the power grid, an oscillating current with a frequency of 10 Hz was generated in the three-phase current of the DFIG stator, which is consistent with the aforementioned oscillation mechanism.

Next, the influence of the SSO frequency change on the corresponding oscillation suppression strategy was analyzed. In this study, the effects of the SSO suppression strategy on a DFIG based on a quasi-resonant controller were investigated with different frequency oscillations. The simulation results are shown in Figure 3.

Figure 3 shows the waveforms of the DFIG stator A-phase output current with oscillation frequencies of 10 Hz and 15 Hz, respectively. Suppose that the oscillation suppression frequency of the resonant controller is 10 Hz, and a quasi-resonant suppression link is added to the RSC control system at 0.7 s. According to Figure 3a, when the grid SSO frequency is 10 Hz, an oscillation component with a frequency of 10 Hz appears in the DFIG stator current. When the simulation was run 0.7 s, a quasi-resonant suppression ring was added into the RSC control system to suppress the internal oscillation of the DFIG system. At this point, the oscillation component of the DFIG output stator current was greatly weakened, and the quasi-resonant controller had a significant effect on SSO suppression. In Figure 3b, the SSO frequency has been changed to 15 Hz, and the oscillation suppression frequency of the quasi-resonant controller is still 10 Hz. In this simulation, an

oscillation component with a frequency of 15 Hz is generated in the DFIG output stator current, and the quasi-resonant controller is also used to suppress the SSO at the same time. As the SSO frequency is beyond the control range of the quasi-resonant controller, the oscillation component of the DFIG stator current is basically not controlled, and the quasi-resonant controller's suppression effect on the SSO is obviously reduced.

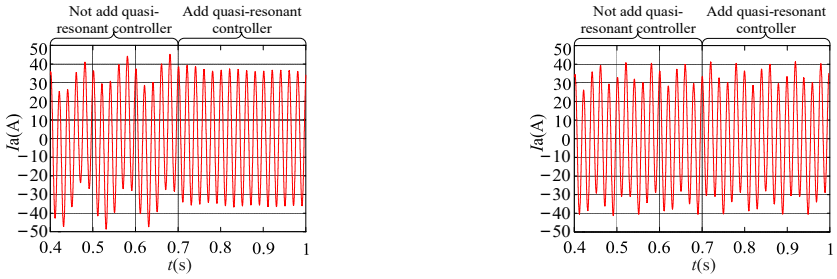

Figure 3. Influence of SSO frequency variation on DFIG system: (**a**) rid oscillation frequency of 10 Hz; (**b**) grid oscillation frequency of 15 Hz.

In conclusion, the generation of a stator sub-synchronous current can disturb the output of the DFIG system, while the change in the oscillation frequency may cause the failure of the SSO suppression strategy within the DFIG system, such that suppression of the SSO at different frequencies is required during SSO suppression.

3. Analysis of SSO Inhibition Mechanism in the DFIG System

After establishing the mathematical model for the RSC under SSO, it is apparent that the stator oscillating current is input into the RSC control system through multiple paths, which increases the difficulty of SSO suppression. Therefore, we used the back-stepping control method to improve the RSC control strategy and reduce the number of SSO propagation paths. In view of the influence of the frequency change in the sub-synchronous current on the SSO suppression strategy, an adaptive quasi-resonant controller was used to suppress the sub-synchronous current component in the RSC system.

3.1. Introduction to the Principle of Back-Stepping Control

At present, the control methods commonly used for nonlinear systems are back-stepping control and sliding mode control. Sliding mode control provides excellent immunity to external random excitation, system parameter variations and unconsidered external disturbances. However, sliding mode control needs to consider the chattering effect of the sliding mode structure, and the greater the amplitude of the control switching, the more obvious the chattering problem is. Most research on wind turbine sliding mode control focuses on improvements to power generation efficiency, often ignoring the system stability problem caused by the change in control strategy during the power tracking process, which easily increases the fatigue load on the system during the control process and reduces the operating life of the wind turbine [19].

In the process of reducing the order of the nonlinear system, the back-stepping method can also reduce errors. Controlling the system through the back-stepping method entails decomposing the more complex high-order system to obtain subsystems with less order compared to the system order. If the back-stepping method is combined with other control algorithms, dynamic control over the controlled system can be achieved despite the interference of unknown disturbance factors [20–22]. Compared with sliding mode control, the design process for a back-stepping controller strictly follows the system stability function and does not consider stability problems such as chattering. The structure of back-stepping controllers is clear, and the dynamic response speed is fast.

Set up the following system:

$$\begin{cases} \dot{x}_{\mathrm{j}} = g_{\mathrm{j}}(\overline{x}_{\mathrm{j}})x_{\mathrm{j}+1} + f_{\mathrm{j}}(\overline{x}_{\mathrm{j}}) \\ \dot{x}_{\mathrm{n}} = g_{\mathrm{n}}(x)u + f_{\mathrm{n}}(x), 1 \le j \le n-1 \\ y = x_1 \end{cases} \tag{3}$$

In Equation (3), $\overline{x}_{\mathrm{j}}$ represents the state variable, and $\overline{x}_{\mathrm{j}} = (x_1, x_2, \cdots, x_{\mathrm{j}})^T$; g_{j} and f_{j} represent continuous functions; u represents the input control variable of the system; and y represents the system output variable.

When using the back-stepping method, it is necessary to design a virtual control variable (e.g., $x_{2\mathrm{d}}$) for the control of the subsystem. Then, the error is set to e_1 and a Lyapunov function is designed:

$$\begin{cases} e_1 = x_1 - x_{\mathrm{d}} \\ V_1 = \frac{1}{2}e_1^2 \end{cases} \tag{4}$$

where x_1 is the system output, x_{d} is the output target value, and V_1 is the Lyapunov function used to determine the stability of the system.

It is necessary to determine the dummy control variables that make the derivative of the Lyapunov function less than zero, as follows:

$$\begin{cases} \dot{V}_1 = e_1 \cdot \dot{e}_1 = e_1 \cdot [g_1(\overline{x}_1)x_{2\mathrm{d}} + f_1(\overline{x}_1) - \dot{x}_{\mathrm{d}}] \\ x_{2\mathrm{d}} = [\dot{x}_{\mathrm{d}} - f_1(\overline{x}_1) - k_1 e_1]g_1(\overline{x}_1)^{-1} \end{cases} \tag{5}$$

$x_{2\mathrm{d}}$ can make x_1 approach and stabilize at x_{d}, and the virtual control variables $x_{3\mathrm{d}}$, $x_{4\mathrm{d}}$, $\cdots$, u of other subsystems can be calculated with the same method, so that x_2, x_3, $\cdots$, x_{n} are gradually stabilized at $x_{2\mathrm{d}}$, $x_{3\mathrm{d}}$, $\ldots$, x_{nd}. Finally, all state variables in the system are eventually tracked smoothly. The above process is recursive across the whole system, so that all subsystems can achieve stable tracking and, finally, all the virtual control variables can be integrated to realize the design of the complete control rate.

3.2. Back-Stepping Control Design Based on DFIG Decoupling Model

Traditional RSC controls use PI controllers, but the control performance of PI controllers is poor when a grid oscillates, so they cannot track the command value. Moreover, when an RSC current loop uses a PI controller, it is necessary to calculate the amount of decoupling compensation in order to eliminate the coupling relationship between the d- and q-axis components of the rotor current and realize independent control over active and reactive power. When the grid sub-synchronous current is input into the DFIG system, the amount of decoupling compensation in the inner loop of the RSC current is disturbed, resulting in the failure of decoupling. Therefore, it is necessary to decouple the RSC control model, which can not only eliminate the influence of the disturbance of the decoupling compensation in the case of oscillation, reducing the number of SSO propagation paths, but also facilitate the design of a back-stepping controller that can improve the system stability.

The DFIG control model decoupling process is shown in Appendix A. The back-stepping method is adopted to control the decoupled DFIG system. Assume that $-\frac{n_{\mathrm{p}}L_{\mathrm{m}}U_{\mathrm{s}}}{J\omega_1 L_{\mathrm{s}}} = \gamma$, $\frac{\sigma L_{\mathrm{r}}L_{\mathrm{m}}U_{\mathrm{s}}}{\omega_1 L_{\mathrm{s}}} = \mu$, $\frac{D}{J} = F$, $\frac{T_{\mathrm{L}}}{J} = T$ and $\sigma L_{\mathrm{r}} = g$. Equation (A8) in Appendix A can then be rewritten as:

$$\begin{cases} \dot{\widetilde{i}}_{\mathrm{rd}} = -\mu\omega_{\mathrm{s}} + gu^*_{\mathrm{rd}} \\ \dot{\widetilde{i}}_{\mathrm{rq}} = gu^*_{\mathrm{rq}} \\ \dot{\omega}_{\mathrm{r}} = \gamma\widetilde{i}_{\mathrm{rd}} - F\omega_{\mathrm{r}} + T \end{cases} \tag{6}$$

Let i_{rd}^* and i_{rq}^* be the instruction values of the d and q components of the rotor current, respectively. According to the form of Equation (4), the error relationship between the actual value and the expected value can be obtained as shown in Equation (7):

$$\begin{cases} e_1 = \widetilde{i}_{rd} - i_{rd}^* \\ e_2 = \widetilde{i}_{rq} - i_{rq}^* \end{cases} \tag{7}$$

Taking the derivation of Equation (7), we get:

$$\begin{cases} \dot{e}_1 = \dot{\widetilde{i}}_{rd} - \dot{i}_{rd}^* = -\mu\omega_s + gu_{rd}^* \\ \dot{e}_2 = \dot{\widetilde{i}}_{rq} - \dot{i}_{rq}^* = gu_{rq}^* \end{cases} \tag{8}$$

For the e_1 construction states of Equations (7) and (18):

$$\begin{aligned} \dot{e}_1 &= -k_1 e_1 + k_1 e_1 + gu_{rd}^* - \mu\omega_s \\ &= -k_1 e_1 + gu_{rd}^* - \mu\omega_s + k_1\widetilde{i}_{rd} - k_1 i_{rd}^* \end{aligned} \tag{9}$$

Constructing the u_{rd}^* control rate:

$$gu_{rq}^* = k_1 i_{rd}^* - k_1\widetilde{i}_{rd} + \mu\omega_s \tag{10}$$

and therefore: $u_{rq}^* = \frac{k_1}{g}(i_{rd}^* - \widetilde{i}_{rd}) + \frac{\mu\omega_s}{g}, k_1 > 0$.

In the above equation, k_1 is the control gain, and the Lyapunov function is constructed according to Equation (4).

$$\lambda_1 = \frac{1}{2}e_1^2 \tag{11}$$

In accordance with Equation (5), we can take the derivative of Equation (11) and insert Equations (9) and (10) into Equation (11) to obtain the following formula:

$$\dot{\lambda}_1 = -k_1 e_1^2 \le 0 \tag{12}$$

It can be seen that $\lambda_1 \ge 0$ and $\dot{\lambda}_1 \le 0$; the subsystem is stable and can control the rotor d-axis current $\widetilde{i}_{rd}$.

The same process is used for the e_2 construction states in Equations (7) and (8):

$$\dot{e}_2 = -k_2 e_2 + k_2 e_2 + gu_{rq}^* = -k_2 e_2 + gu_{rq}^* + k_2\widetilde{i}_{qr} - k_2 i_{qr}^* \tag{13}$$

Constructing u_{rq}^* control rate:

$$gu_{rq}^* = k_1 i_{qr}^* - k_1\widetilde{i}_{qr} \tag{14}$$

and therefore: $u_{rq}^* = \frac{k_2}{g}(i_{qr}^* - \widetilde{i}_{qr}), k_2 > 0$.

In the above equation, k_2 is the control gain, and the Lyapunov function is constructed according to Equation (4).

$$\lambda_2 = \frac{1}{2}e_2^2 \tag{15}$$

In accordance with Equation (8), we can take the derivative of Equation (15), and substitute Equations (13) and (14) into it:

$$\dot{\lambda}_2 = -k_2 e_2^2 \le 0 \tag{16}$$

It can be seen that $\lambda_2 \ge 0$ and $\dot{\lambda}_2 \le 0$; the subsystem is stable and can control the rotor q-axis current $\widetilde{i}_{rq}$.

Under the control rate described by Equations (10) and (14), the following equation can be obtained using Equations (9) and (13):

$$\begin{cases} \dot{e}_1 = -k_1 e_1 \\ \dot{e}_2 = -k_2 e_2 \end{cases} \tag{17}$$

The Lyapunov function is constructed from Equations (4) and (17):

$$\lambda = \frac{1}{2}e_1^2 + \frac{1}{2}e_2^2 \tag{18}$$

In accordance with Equation (5), the derivation of Equation (18) can be obtained:

$$\dot{\lambda} = -k_1 e_1^2 - k_2 e_2^2 \leq 0 \tag{19}$$

It can be seen from Equations (18) and (19) that, under the control of the control rate described by Equations (10) and (14), the RSC control system is stable. Therefore, the controller designed according to Equations (10) and (14) can meet the stability requirements for the DFIG system under oscillation. At the same time, the design of the control rate simplifies the control strategy for traditional RSC systems and reduces the number of paths of the oscillation input into the RSC control system. The SSO is only input into the RSC system through the power outer loop and the current inner loop and the sub-synchronous component does not need to be considered in the feedforward decoupling compensation amount.

3.3. Quasi-Resonant Controller

In this study, an RSC back-stepping controller was designed based on the DFIG decoupling model, simplifying the RSC control strategy. Although the back-stepping controller design could meet the system stability requirements, it did not completely suppress the sub-synchronous disturbance in the RSC system, so it was difficult make the output of the DFIG system converge to the expected value. In order to realize the suppression of the stator sub-synchronous current by the DFIG system, an adaptive quasi-resonant controller was used to track the stator sub-synchronous current, and the control voltage output by the quasi-resonant controller was input into the RSC control system.

The transfer function of the quasi-resonant controller is shown in Equation (20) [23,24]:

$$G(s) = \frac{2K_R\omega_c s}{s^2 + 2\omega_c s + \omega_0^2} \tag{20}$$

In Equation (20), K_R is the gain coefficient, ω_c is the cutoff frequency and ω_0 is the signal frequency that the quasi-resonant controller needs to control.

A Bode diagram was used to analyze the performance of the resonant controller described by Equation (20), with ω_0 set to 50 Hz, and the result is shown in Figure 4.

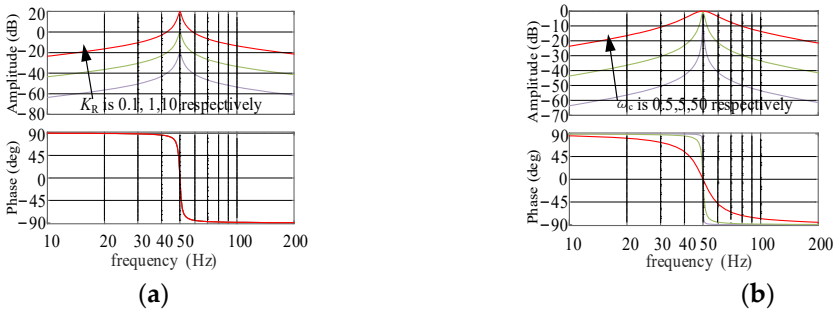

Figure 4. Bode diagrams of G(*s*) as K_R and ω_c change: (**a**) the value of K_R changes; (**b**) the value of ω_c changes.

It can be seen from Figure 4 that, when ω_c is a fixed value, the amplitude gain in the quasi-resonant controller is positively correlated with the magnitude of K_R. When K_R is a fixed value, the amplitude and phase of the quasi-resonant controller tend to be flat with the increase of ω_c; that is, the magnitude of ω_c is negatively correlated with the influence of $G(s)$, which is affected by the frequency change. However, no matter how ω_c and K_R change, when ω_0 is determined, the quasi-resonant observation control has the best tracking effect on this frequency signal. Therefore, it is feasible to use the quasi-resonant controller to control the SSO component in the DFIG system.

Traditional quasi-resonant controllers only control AC signals of specific frequencies. However, when the input signal frequency deviates greatly from the control frequency ω_0, the gain provided by the quasi-resonant controller is greatly reduced. An adaptive algorithm is required for sub-synchronous current frequency changes.

A simplified transformation of Equation (20) can be obtained as follows:

$$G(s) = \frac{Hs}{s^2 + HKs + MH} \tag{21}$$

In the equation, $H = 2K_R\omega_c$, $K = \frac{1}{K_R}$ and $M = \frac{\omega_0^2}{2K_R\omega_c}$.

It can be seen from Equation (21) that the value of the parameter M is directly related to the frequency of the control target signal; that is, M directly determines the tracking of the input signal frequency by the quasi-resonant controller. Therefore, the key link in designing a frequency-adaptive quasi-resonant controller is realizing the real-time adjustment of M when the frequency of the input signal changes through an adaptive design. At this time, the adaptive quasi-resonant controller outputs a control signal that changes with the frequency of the input signal in order to achieve control over the input signal.

4. SSO Suppression Strategy for DFIG System

4.1. Design of SSO Suppression Strategy for DFIG System

From the mathematical model of the RSC control with SSO, it can be deduced that the voltage command value output by the RSC controller under the oscillation condition can be expressed as:

$$\begin{cases} u_{rd}^* = u_{rd0}^* + u_{rd\_sub}^* \\ u_{rq}^* = u_{rq0}^* + u_{rq\_sub}^* \end{cases} \tag{22}$$

When the SSO is input into the DFIG system, the sub-synchronous current component in the stator current has the most serious impact on the RSC control system. To suppress the sub-synchronous component in the DFIG stator current, the output voltage command value of the RSC controller in the d-q coordinate system should be divided into two parts. One part comprises the fundamental wave components u_{rd0}^* and u_{rq0}^* and the other part comprises the secondary synchronous components $u_{rd0\_sub}^*$ and $u_{rq0\_sub}^*$. The fundamental wave component is the DC component, and the secondary synchronous component is the AC component. u_{rd0}^* and u_{rq0}^* can control the active and reactive power output by the DFIG, and $u_{rd0\_sub}^*$ and $u_{rq0\_sub}^*$ need to achieve the suppression of the sub-synchronous component in the DFIG stator current.

In the previous analysis, the back-stepping controller could control the fundamental components u_{rd0}^* and u_{rq0}^*. The AC components $u_{rd0\_sub}^*$ and $u_{rq0\_sub}^*$ were controlled by a quasi-resonant controller. In order to suppress the frequency-varying sub-synchronous current, an adaptive quasi-resonant controller can be used to track it. By optimizing the RSC control strategy, a back-stepping SSO suppression strategy can be designed for the adaptive quasi-resonant controller. The control block diagram is shown in Figure 5.

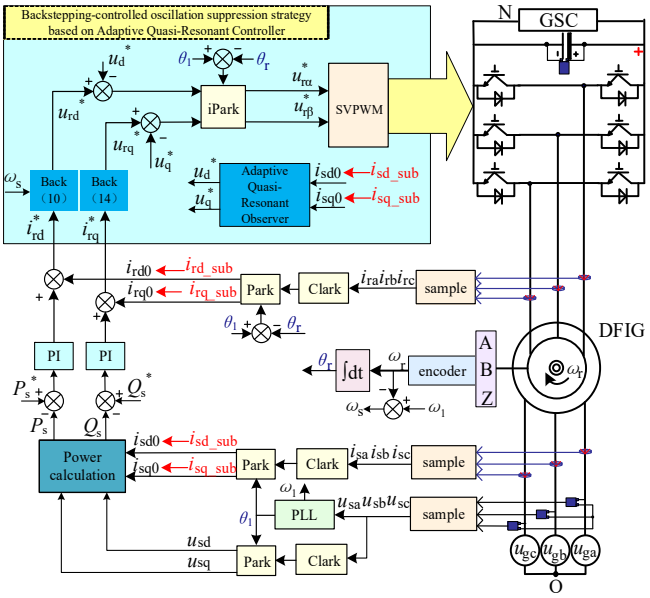

Figure 5. Back-stepping SSO suppression strategy based on adaptive quasi-resonant controller.

The synergistic process of the RSC controller and quasi-resonant controller with SSO occurs as follows: when oscillation occurs, the rotor d-axis current $\widetilde{i}_{rd}$ and q-axis current $\widetilde{i}_{rq}$ containing oscillation components are input into the back-stepping controller and, at the same time, the collected synchronous angular frequency ω_1 and rotor angular frequency ω_r are input into the back-stepping controller. The rotor voltage control commands u^*_{rd} and u^*_{rq} are obtained through the calculations of the back-stepping controller. u^*_{rd} and u^*_{rq} can realize decoupling control over the DFIG output active and reactive power.

Due to the existence of the oscillating current, it is difficult for the back-stepping controller to make the DFIG output converge to the desired value. In order to suppress the stator sub-synchronous current, a direct resonant control was adopted in this study [25]. The stator current d and q components are input into the adaptive quasi-resonant controller, and the resonant controller controls the oscillating current. Since the resonance controller has no adjustment effect on the DC component, the final output resonance control voltages u^*_d and u^*_q can only control the corresponding stator oscillation current. Through the RSC current control, u^*_d and u^*_q interact with the sub-synchronous resonant electromotive force induced on the rotor side of the DFIG to generate a sub-synchronous harmonic current, thereby suppressing the sub-synchronous current in the DFIG stator and realizing the sinusoidal output of the stator current. The synergy of the RSC current controller and the adaptive quasi-resonant controller ensures that the RSC is not disturbed by the oscillation and can still maintain the normal operation of the DFIG when grid SSO occurs.

4.2. Improved Controller Performance Analysis

The basic principle of the control strategy proposed in this paper is explained in the analysis in Section 4.1. This section analyzes the control performance of the strategy for sub-synchronous oscillation of a power grid.

When the grid voltage is oriented along the d-axis, Equations (23) and (24) can be obtained from the model of the DFIG:

$$\begin{cases} u_{sd} = |u_s| = U_s \approx -\omega_1 \psi_{sq} \\ u_{sq} = 0 \approx \omega_1 \psi_{sd} \end{cases} \tag{23}$$

$$\boldsymbol{I}_{sdq} = \frac{1}{L_s}\boldsymbol{\psi}_{sdq} - \frac{L_m}{L_s}\boldsymbol{I}_{rdq} \tag{24}$$

where u_{sd} is the d-axis component of the grid voltage vector; u_{sq} is the grid voltage of the q-axis component; u_s is the grid voltage vector; U_s is the grid voltage vector magnitude; ω_1 is the rotational angular velocity of the grid voltage vector; ψ_{sq} is the q-axis component of the flux linkage vector; ψ_{sd} is the d-axis component of the flux linkage vector; $\boldsymbol{I}_{sdq}$ is the dq-axis component of the stator current; L_s is the stator inductance; L_m is the mutual inductance between the stator and rotor; and $\boldsymbol{I}_{rdq}$ is the dq-axis component of the rotor current.

The block diagram for the RSC current vector control embedded in the adaptive quasi-resonant (R) and back-stepping controller is shown in Figure 6.

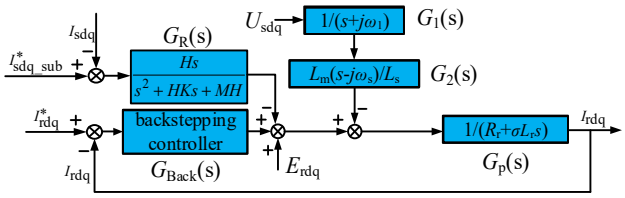

Figure 6. Block diagram of the rotor current vector control embedded in the adaptive quasi-resonant and back-stepping controller.

In the case of grid voltage orientation, utilizing Figure 6 and Equations (23) and (24), the equivalent transfer function of an RSC based on adaptive quasi-resonance and back-stepping control strategies can be written as:

$$I_{sdq} = F_1(s)U_{sdq} + H_1(s)I^*_{rdq} \tag{25}$$

In the vector control of the d-axis grid voltage, we only consider the characteristics for the protection of the DFIG wind power system against sub-synchronous harmonic voltage disturbance along the d-axis. In the block diagram for the current vector control embedded in the adaptive quasi-resonant and back-stepping controller, $F_1(s)$ is used to measure the disturbance on the forward channel of the DFIG; that is, the anti-disturbance capability of the sub-synchronous harmonic voltage. $H_1(s)$ is used to represent the dynamic response capability of the current loop. From Figure 6, the following equation can be deduced:

$$F_1(s) = \frac{G_1(s)/L_s + G_1(s)G_{back}(s)G_P(s)/L_s + G_1(s)G_2(s)G_P(s)L_m/L_s}{1 + G_{back}(s)G_P(s) + G_R(s)G_P(s)L_m/L_s} \tag{26}$$

$$H_1(s) = \frac{G_{back}(s)G_P(s)L_m/L_s}{1 + G_{back}(s)G_P(s) + G_R(s)G_P(s)L_m/L_s} \tag{27}$$

We can substitute $F_1(s)$ and $H_1(s)$ into the parameters of Table 1 to draw the Bode diagrams of $F_1(s)$ and $H_1(s)$, as shown in Figures 7 and 8.

Table 1. DFIG experimental platform-related parameters.

Parameter	Value	Parameter	Value
Rated power	15 kW	Rotor leakage reactance $L_{r\sigma}$	0.0022 H
Stator voltage	200 V	Moment of inertia of the motor J	0.39 Kg·m^2
Mutual inductance resistance L_m	0.0427 H	Pole logarithm of motor n_p	3
Stator resistance R_s	0.379 Ω	DC side voltage V_{dc}	400 V
Stator leakage reactance $L_{s\sigma}$	0.0011 H	Inductance into the line L_g	0.005 H
Rotor resistance R_r	0.314 Ω	Motor magnetic flux leakage coefficient σ	0.07288
Rated frequency	50 Hz	DC bus capacitance C	2200 μF

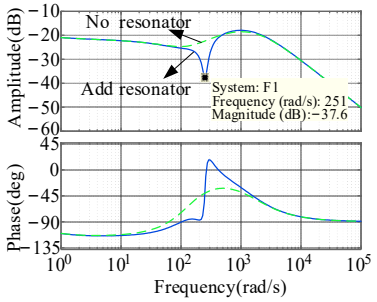

Figure 7. Frequency response of RSC $F_1(s)$ based on resonant control.

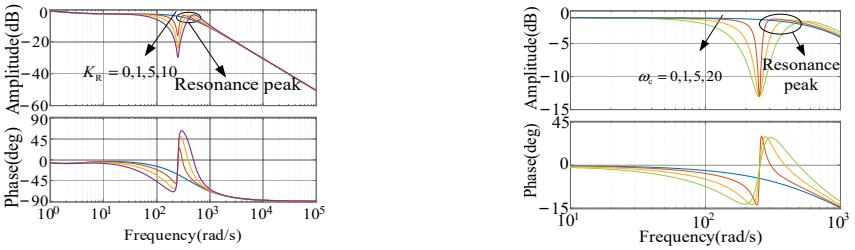

Figure 8. Frequency response of RSC $H_1(s)$ based on resonant control: (**a**) frequency response of $H_1(s)$ when K_R changes; (**b**) frequency response of $H_1(s)$ when ω_c changes.

Figure 7 shows the Bode diagram of the frequency response of $F_1(s)$. For the DFIG wind power system, the amplitude gain of $F_1(s)$ at the sub-synchronous resonance frequency should be as small as possible; this allows the anti-disturbance ability of the sub-synchronous voltage component in the power grid to be improved. It is not difficult to see from Equation (25) that the influence of the sub-synchronous voltage U_{sdq_sub} on the stator current I_{sdq} is affected by $F_1(s)$: the smaller the amplitude of $F_1(s)$ is, the smaller the interference of the sub-synchronous harmonic voltage with the DFIG system and the greater the robustness of the system. As can be seen from Figure 7, the amplitude gain in the improved controller at the resonant frequency is significantly smaller than the amplitude gain at other frequencies of the curve and, compared with when a resonant controller is not used, the amplitude gain at the resonance point is reduced by about 14 dB, which confirms that, in the case of sub-synchronous oscillation, a resonant controller can effectively reduce the effect of the sub-synchronous harmonic voltage on the influence of the generator stator current. Therefore, the proposed strategy based on adaptive quasi-resonant RSC back-stepping control has a strong anti-disturbance capability with regard to sub-synchronous voltages, which can significantly enhance the robustness of the system.

For the dynamic response of the current, it can be seen from Figure 8 that, when K_R or ω_c increases, the amplitude of the rotor current of the DFIG control system decreases, resulting in a slower dynamic response speed in the current loop. As can be further seen in Figure 8, the rotor current may oscillate due to the appearance of a resonant peak and even cause the system to become unstable. Therefore, the choice of the resonance proportional coefficient K_R and the bandwidth ω_c should be considered as a compromise.

5. Simulation and Experiment

5.1. Simulation Analysis

In this paper, a back-stepping SSO suppression strategy based on an adaptive quasi-resonant controller is proposed. The performance of the RSC current controller had to be simulated and analyzed. Assuming that the initial speed of the DFIG is 900 r/min, the expected value of DFIG output active power will be 4000 W at this time, while the expected value of the DFIG output reactive power will always be 0 Var. The values of the power

output of the DFIG with the improved controller and the PI controller were compared through a simulation. The simulation results are shown in Figure 9.

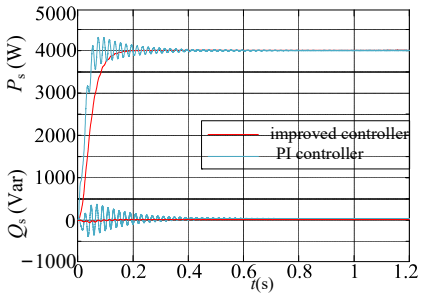

Figure 9. DFIG output power using different controllers.

In order to simulate the unpredictable noise signal during the motor control, a set of random numbers were added to the rotor d and q currents, respectively, and the amplitude was limited to within 5% of the actual current component. It can be seen from Figure 9 that both the improved controller and the PI controller could control the DFIG output power and make it reach the desired value. However, due to the interference of the noise signal, the DFIG power controlled by the PI controller exhibited an overshoot and oscillation phenomenon, and it took a period of time to stabilize the DFIG output at the desired value. However, there was no integral link in the back-stepping controller, so it was not necessary to consider the problem of integral saturation. The outputs of the DFIG controlled by the two controllers were smooth; less affected by small disturbances, such as noise signals; and could converge to the target value quickly.

Figure 10 shows the improved controller's tracking of changes in power. The simulation condition is that, at 0.5 s, the expected value of the DFIG output active power changed from 4000 W to 4500 W. It can be seen from the simulation results that, when the expected value of the active power changed suddenly, the DFIG active power controlled by the back-stepping controller changed to the expected value, which was reached after 0.1 s~0.2 s. In this process, the output reactive power of the DFIG is still 0 VAR, which verifies that the RSC controlled by the improved controller could realize power decoupling control of the DFIG.

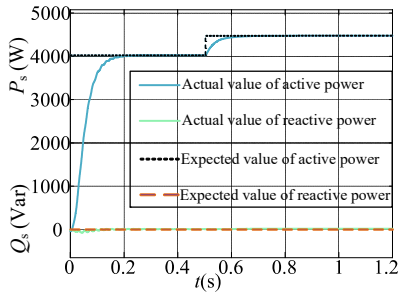

Figure 10. DFIG output power at rotor speed jump.

Next, the oscillation suppression effect of the back-stepping SSO suppression strategy based on the adaptive quasi-resonant controller was verified at different SSO frequencies.

Figure 11 compares the adaptive quasi-resonant controller with the quasi-resonant controller, verifying that the adaptive quasi-resonant controller could still achieve the control target when the SSO frequency changed. The adaptive quasi-resonant controller was used with an oscillation frequency of 10 Hz, while that of the resonant controller was 30 Hz. Figure 11 shows that, with an oscillation frequency of 10 Hz, since the control frequency of the quasi-resonant controller was fixed at 30 Hz, the oscillation frequency deviated significantly from the control range of the controller, so the quasi-resonant controller no

longer exerted a suppression effect on the sub-synchronous current. When the adaptive quasi-resonant controller was used, the control frequency of the controller changed with the oscillation frequency, so the frequency change in the sub-synchronous current did not affect the performance of the adaptive quasi-resonant controller.

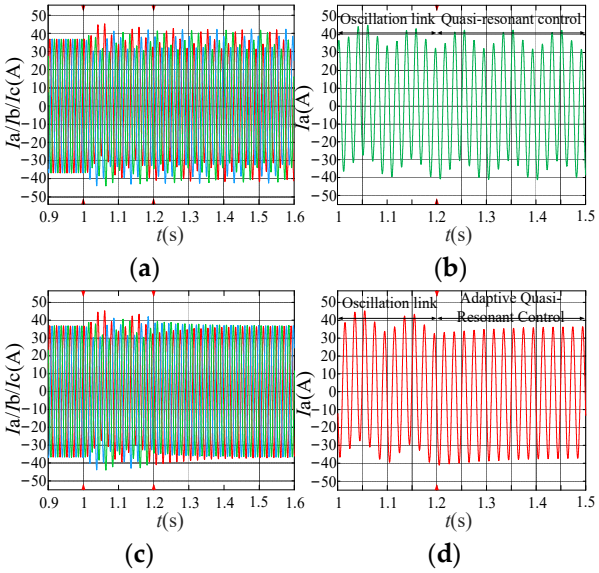

Figure 11. Comparison of inhibition effects between two resonant controllers with SSO frequency of 10 Hz: (**a**) quasi-resonant controller; (**b**) stator current single phase magnification; (**c**) adaptive quasi-resonant controller; (**d**) stator current single phase magnification.

Finally, the DFIG stator power and capacitance voltage waveforms before and after SSO inhibition were observed. The expected values for the stator active power and reactive power were 4000 W and 0 Var, and the capacitance voltage was maintained at 400 V.

As shown in Figure 12, when the power grid SSO was generated, both the DFIG stator side output power and the capacitance voltage oscillated, with the power oscillation being the most severe. When the oscillatory inhibition strategy proposed here was adopted, the DFIG stator-side reactive power oscillation was basically suppressed and, while the active power still oscillated, the amplitude of the oscillation was reduced by nearly 60% compared with before the inhibition. After being subjected to the control of the adaptive quasi-resonant controller, the sub-synchronous component in the DC bus voltage was also reduced. As the DFIG grid side was still affected by the SSO, the oscillation was still generated in the DC bus voltage, but the impact of the DC bus voltage fluctuation on the RSC control was weaker.

In summary, the simulation analysis verified the effectiveness of the control strategy proposed in this paper. In the case of uncertain perturbations in the system, the response speed controlled by the improved controller was faster than that of a traditional PI control, and the DFIG output power could be adjusted quickly and smoothly. The adaptive quasi-resonant controller showed a good inhibition effect on the SSO component in the DFIG stator current, and when the SSO frequency of the grid changed, the SSO frequency could be tracked and the variable frequency SSO component could be suppressed.

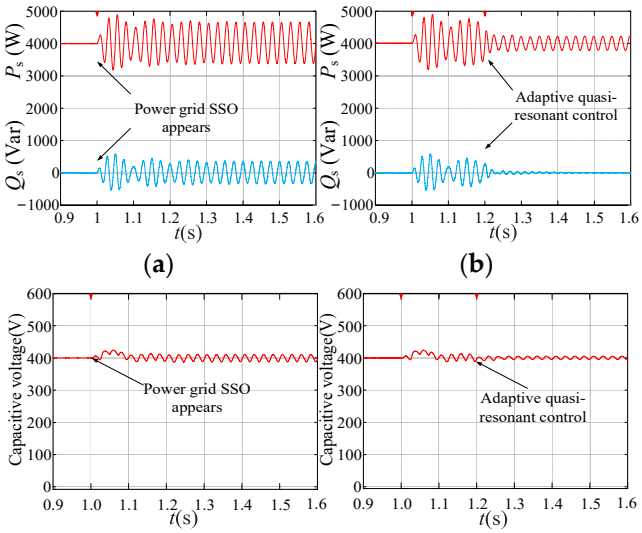

Figure 12. Comparison of stator power and capacitance voltage waveforms before and after SSO suppression: (**a**) power before the SSO inhibition; (**b**) power after the SSO inhibition; (**c**) V_{dc} before the SSO inhibition; (**d**) V_{dc} after the SSO inhibition.

5.2. Experimental Verification

In order to verify the actual effect of the SSO suppression strategy, experimental verification of the strategy proposed in this paper was carried out using a model platform based on a 15 kVA doubly-fed wind power system. The layout of the experimental platform is shown in Figure 13 and a detailed illustration of each part of the experimental platform is shown in Figure 14.

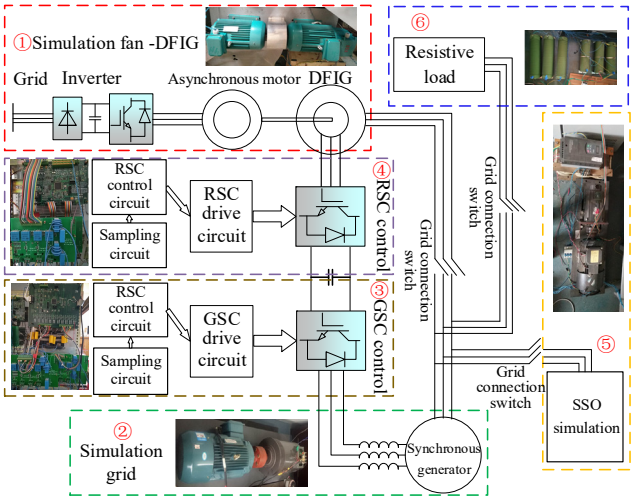

Figure 13. Layout diagram of experimental platform for a DFIG system.

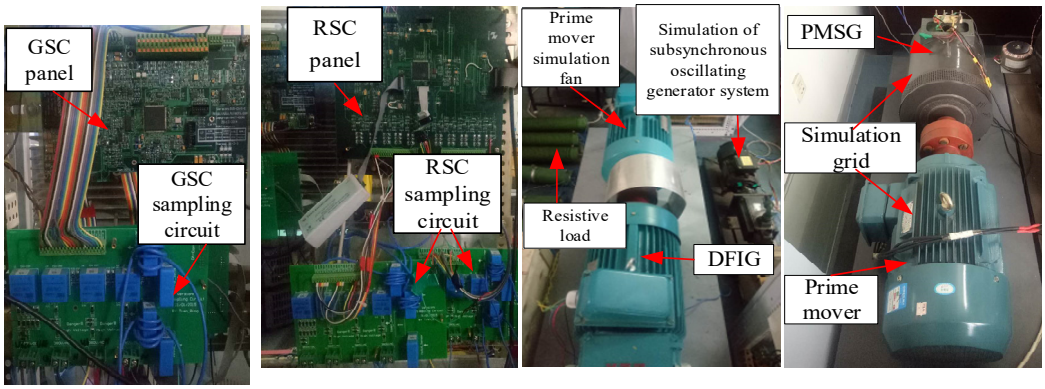

Figure 14. Experimental platform for the oscillatory inhibition of the DFIG system: (**a**) GSC experiment platform; (**b**) RSC experiment platform; (**c**) DFIG power generation device; (**d**) simulation power grid platform.

The DFIG experimental platform was composed of a GSC, an RSC, a simulated power grid and an SSO simulation system. The RSC and GSC control systems both used DSPF28335 as the control chip. The permanent magnet synchronous motor was driven by the prime mover to generate sub-synchronous voltage, which was merged into the simulated power grid through the transformer, thereby simulating the experimental environment for the grid SSO. The experimental parameters are shown in Table 1.

Before the experiment, it was necessary to check whether the DFIG met the grid connection requirements. The DFIG stator A-phase voltage and the simulated grid A-phase voltage waveforms before the grid connection are shown in Figure 15. As shown in the figure, the DFIG stator voltage and the grid voltage basically had the same amplitude, phase, frequency and phase sequence, so the DFIG system could be connected to the grid.

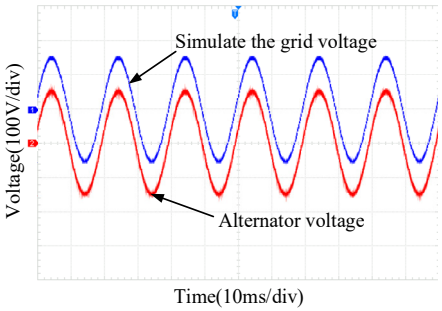

Figure 15. Output voltage waveforms for the grid and DFIG before grid connection.

Figure 16 shows the DFIG stator and rotor current waveforms at different speeds. The rotor speeds were set to 900 r/min and 1200 r/min, respectively; that is, the motor ran in sub-synchronous and super-synchronous states. By observing the rotor A-phase current and stator A-phase current, it could be seen that, at different speeds, the rotor current frequency of the DFIG also changed correspondingly, while the stator current was always kept at 50 Hz. The experiment proved that the DFIG system controlled by the back-stepping controller and the proportional controller could achieve constant-frequency variable speed control.

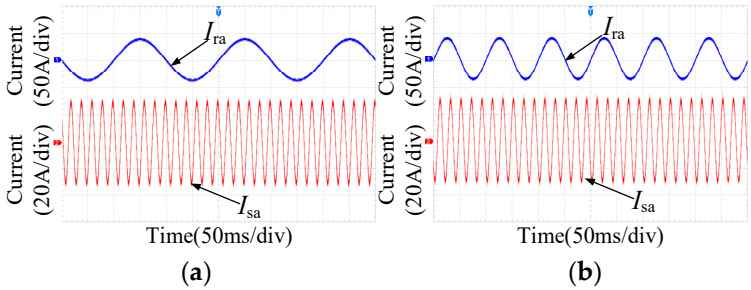

Figure 16. The DFIG determining the rotor current at different speeds: (**a**) rotor speed of 900 r/min; (**b**) rotor speed of 1200 r/min.

The results for the SSO suppression experiments are shown in Figures 17–19. In the experiments, the prime mover was selected to drive the PMSG to simulate the generation of the grid oscillation voltage. The amplitude of the sub-synchronous voltage was 10% of the simulated grid voltage, and the frequencies were 30 Hz, 20 Hz and 10 Hz, respectively. The rotor speed was fixed at 900 r/min, and the motor was run in a sub-synchronous state. The motor speed, the simulated SSO voltage waveform, the simulated grid voltage waveform when the oscillation occurred and the DFIG stator and rotor current waveforms before and after the oscillation suppression were obtained by the sampling circuit.

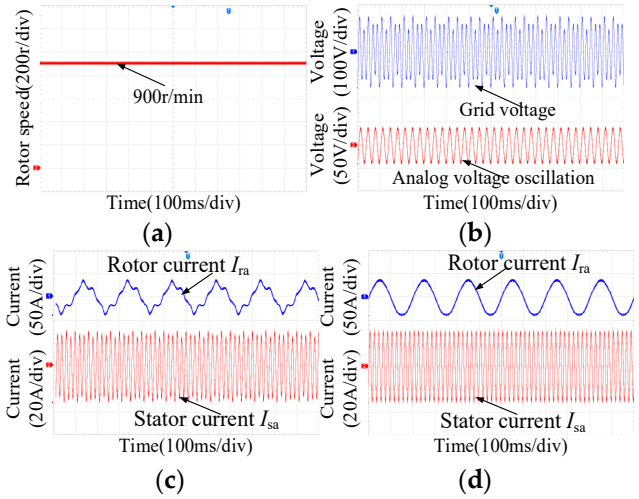

Figure 17. The oscillation suppression suppressed-contrast waveforms at SSO frequency of 30 Hz: (**a**) DFIG rotor speed; (**b**) grid voltage oscillation waveform; (**c**) before oscillation suppression; (**d**) after oscillation suppression.

By comparing the experimental results for the grid SSO frequencies of 30 Hz, 20 Hz and 10 Hz, it can be seen that, when the grid voltage SSO was generated, the stator and rotor currents in the DFIG were disturbed accordingly, and the DFIG output also oscillated. With the use of the adaptive quasi-resonant controller to control the SSO, the oscillatory components in the stator and rotor currents were clearly suppressed, thus facilitating the sinusoidal output of the stator current and maintaining the stable operation of the DFIG.

Next, a comparative analysis of the oscillation control effects of the adaptive quasi-resonant controller and the quasi-resonant controller was carried out to verify the effectiveness of the two resonant controllers in suppressing oscillation when the SSO frequency was abruptly changed. The experimental results are shown in Figure 20.

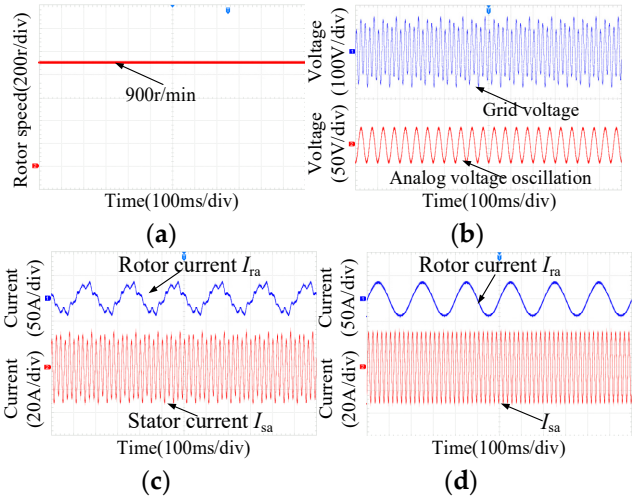

Figure 18. The oscillation suppression suppressed-contrast waveforms at SSO frequency of 20 Hz: (**a**) DFIG rotor speed; (**b**) grid voltage oscillation waveform; (**c**) before oscillation suppression; (**d**) after oscillation suppression.

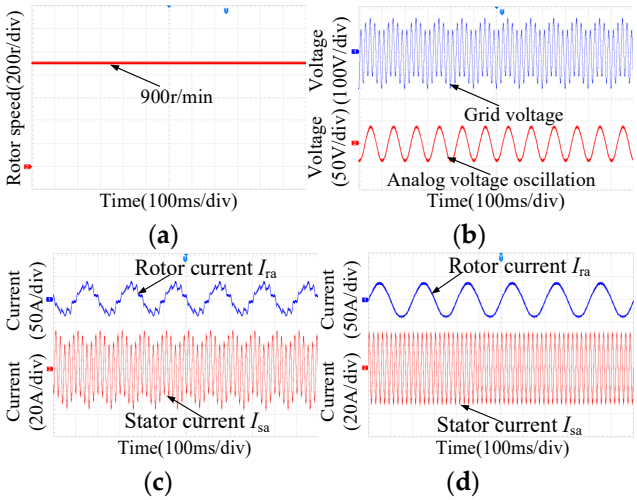

Figure 19. The oscillation suppression suppressed-contrast waveforms at SSO frequency of 10 Hz: (**a**) DFIG rotor speed; (**b**) grid voltage oscillation waveform; (**c**) before oscillation suppression; (**d**) after oscillation suppression.

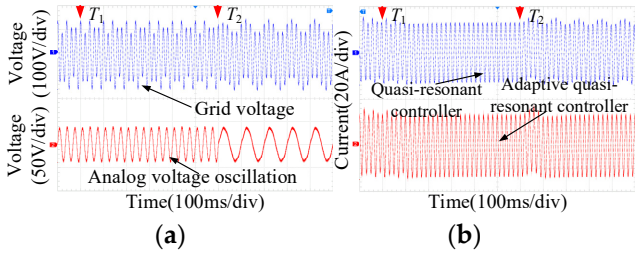

Figure 20. Comparison of the waveforms of the oscillation suppression effects of the two resonant controllers: (**a**) grid voltage oscillation waveform; (**b**) stator current waveform comparison.

In Figure 20, the initial value of the simulated sub-synchronous voltage frequency was 30 Hz, and the oscillation amplitude was the same as the experiment described above. At time T_1, the quasi-resonant controller and the adaptive quasi-resonant controller were respectively put into control. By observing the stator current, it could be seen that, after

the two resonant controllers were put into use, the oscillation component in the DFIG stator current was significantly weakened, and both controllers could suppress the 30 Hz sub-synchronous current. However, at T_2, the SSO frequency suddenly changed to 10 Hz, while the oscillation amplitude did not change. At this time, the control frequency of the quasi-resonant controller was 30 Hz, but the frequency of the sub-synchronous current suddenly exceeded its control range, and a corresponding 10 Hz oscillation component appeared in the stator current after time T_2. The adaptive quasi-resonant controller could still control the sub-synchronous current after the oscillation frequency switched. After the changed sub-synchronous voltage frequency was maintained for about 100 ms, the oscillation component in the stator current was suppressed, and the DFIG stator current returned to the sinusoidal output. This experiment confirmed that the adaptive quasi-resonant controller could control the broadband DFIG stator sub-synchronous current, which proves that the SSO suppression strategy proposed in this paper is effective.

Finally, the inhibition effect of the proposed SSO inhibition strategy was verified. The rotor speed was increased from 800 r/min to 1200 r/min, and the SSO inhibition link performed RSC control at 840 r/min and 1060 r/min, respectively. The oscillatory components in the stator current were observed, and the experimental results are shown in the following Figure 21.

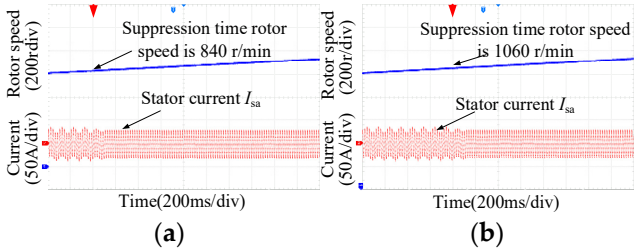

Figure 21. The SSO inhibition effect at different speeds: (**a**) sub-synchronous speed; (**b**) super-synchronous speed.

It can be seen that, when the SSO inhibition of DFIG was run at sub-synchronous and super-synchronous speeds, both the sub-synchronous components in the stator current could be effectively suppressed, and the change in the rotor speed had no effect on the control exerted by the adaptive quasi-resonant control. This experiment demonstrated that the SSO inhibition strategy could satisfy the dynamic response requirements of the DFIG.

Furthermore, FFT spectrum analysis was carried out on the stator current when the SSO frequency changed, and the harmonic content in the stator current was observed when the quasi-resonant controller and adaptive quasi-resonant controller were used to suppress the stator sub-synchronous current. The specific results are shown in Figure 22.

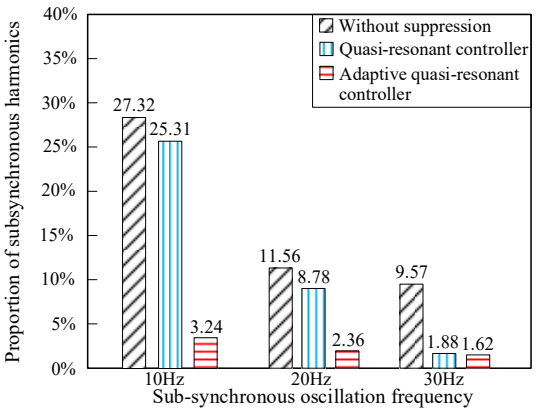

Figure 22. The results of the FFT spectrum analysis of the DFIG stator current.

As can be seen from Figure 22, when the grid SSO frequencies were 10 Hz, 20 Hz and 30 Hz, respectively, the proportions of sub-synchronous harmonics in the DFIG stator current were 27.32%, 11.56% and 9.57%, respectively. At this time, the rejection frequency of the quasi-resonant controller was 30 Hz, and the harmonics in the stator current were suppressed by the quasi-resonant controller and the adaptive quasi-resonant controller, respectively. From Figure 22, it can be seen that the adaptive quasi-resonant controller could effectively suppress the oscillation component in the stator current at each frequency and reduce the harmonic content in the stator current to less than 5%. However, the quasi-resonant controller could only suppress the sub-synchronous component of the stator current at 30 Hz, and the suppression effect of the quasi-resonant controller gradually weakened as the SSO frequency gradually deviated from the resonant frequency of the quasi-resonant controller. This result confirms that the adaptive quasi-resonant controller could achieve the suppression of the wideband DFIG stator sub-synchronous current, thus confirming the effectiveness of the SSO suppression strategy proposed in this paper.

6. Conclusions

Addressing the problem of grid SSO affecting the stable operation of DFIG systems, and considering the influence of the oscillation frequency change on the SSO suppression strategy, this paper proposed a back-step SSO suppression strategy based on an adaptive quasi-resonant controller. The following conclusions can be drawn from the simulation and experimental research:

(1) The application of the RSC current controller designed based on the back-stepping method could simplify the RSC control strategy and reduce the number of transmission paths in the grid SSO from three to two, and its control effect was better than that of the traditional PI controller. In the case of unknown perturbations in the input signal, the back-stepping controller could quickly achieve the control goal of the RSC and complete the adjustment of the DFIG output power within 0.1 s;

(2) The adaptive quasi-resonant controller could suppress the sub-synchronous current from the input DFIG and reduce the sub-synchronous current of the stator side to less than 5%. When the grid SSO frequency was abruptly changed from 30 Hz to 10 Hz, the adaptive quasi-resonant controller could still respond quickly, maintaining the sinusoidal output of the stator current. The experimental results showed that the adaptive quasi-resonant controller could suppress the sub-synchronous components of different frequencies in the DFIG system.

In summary, this study verified the effectiveness of the proposed SSO suppression strategy through a simulation and experiments. Adopting this strategy can improve the anti-interference ability of DFIG systems subject to the SSO of the power grid and provide a guarantee for their stable operation, which has a certain engineering value.

Author Contributions: Conceptualization, writing—review and editing, supervision, project administration, funding acquisition, D.S.; validation, formal analysis, software visualization, F.M.; methodology investigation, data curation, writing—original draft preparation, W.S.; All authors have read and agreed to the published version of the manuscript.

Funding: This research received no external funding.

Data Availability Statement: Not applicable.

Acknowledgments: Nan WANG, Kai ZHOU and Bo HU.

Conflicts of Interest: The authors declare no conflict of interest.

Appendix A. DFIG Control Model Decoupling

To date, various algorithms have been proposed to solve the problem of coupling different channels in a converter control. One study [26] proposed a d-q current decoupling control method for a single-phase grid-connected converter without a delay. This method took a single-phase pulse width modulation (PWM) converter as its research object. By

improving the orthogonal signal generator, the virtual orthogonal component of the β axis corresponding to the grid current could be generated without a delay. In addition, the reference current signal mutation could be tracked without a delay, improving the dynamic response speed of the system. Another study [27] designed a two degrees of freedom PI controller by analyzing the influence of the converter decoupling control link on the stability of the control system. This method improved the equivalent motor stator resistance, the robustness of the link between the current ring and the decoupling parameters and the response characteristics of the current ring. The above methods can be used to improve the response speed of a control system, but the feedforward decoupling compensation still needs to be introduced into the current internal loop. When grid SSO occurs, the sub-synchronous component is input into the RSC control system through the feedforward decoupling. Therefore, in order to reduce the number of SSO propagation paths, a back-stepping controller was designed, combining state feedback decoupling and back-stepping control, to decouple the RSC current inner loop. The state feedback decoupling can reduce the complexity of the control system, thus simplifying the system equation of state, eliminating the coupling components and facilitating the design of subsequent controllers. The design of the back-stepping controller had to satisfy the stability equation of the system in order to improve the stability of the system. Considering the decoupling control ability of the back-stepping controller for nonlinear systems and that fact that it has no bandwidth limitations, the back-stepping controller can be applied to situations of unknown disturbance in power grids. Therefore, a back-stepping controller based on state feedback decoupling could not only improve the response speed and stability of control systems but also simplify the control strategy of the RSC and reduce the number of propagation paths of the SSO.

Equation (A1) can be obtained from Equation (1) and the equation of motion of the DFIG system. In the equation, J is the moment of inertia of the generator; n_p is the number of pole pairs; D is the damping coefficient; and T_L is the input torque of the wind turbine. $\widetilde{i}_{rd} = i_{rd0} + i_{rd\_sub}$, and $\widetilde{i}_{rq} = i_{rq0} + i_{rq\_sub}$.

$$\begin{cases} \frac{d\widetilde{i}_{rd}}{dt} = -\frac{R_r}{\sigma L_r}\widetilde{i}_{rd} + \omega_s\widetilde{i}_{rq} + \frac{1}{\sigma L_r}u_{rd} - \frac{\omega_s L_m U_s}{\sigma L_r L_s \omega_1} \\ \frac{d\widetilde{i}_{rq}}{dt} = -\omega_s\widetilde{i}_{rd} - \frac{R_r}{\sigma L_r}\widetilde{i}_{rq} + \frac{1}{\sigma L_r}u_{rq} \\ \dot{\omega}_r = -\frac{n_p L_m U_s}{J\omega_1 L_s}\widetilde{i}_{rd} - \frac{D}{J}\omega_r + \frac{T_L}{J} \end{cases} \tag{A1}$$

Analysis of Equation (A1) shows that the state equation of the DFIG system is a third-order equation, and there is a coupling relationship between the first-order differential equations of $\widetilde{i}_{rd}$ and $\widetilde{i}_{rq}$.

We can rewrite the two equations related to $\widetilde{i}_{rd}$ and $\widetilde{i}_{rq}$ in Equation (A1) into matrix form and use $\widetilde{i}_{rd}$ and $\widetilde{i}_{rq}$ as the output, so that we have:

$$\begin{cases} \dot{\boldsymbol{I}} = \boldsymbol{A}\boldsymbol{I} + \boldsymbol{B}\boldsymbol{U} \\ \boldsymbol{Y} = \boldsymbol{C}\boldsymbol{I} \end{cases} \tag{A2}$$

In Equation (A2), $\boldsymbol{A}$ is the system matrix, $\boldsymbol{B}$ is the control matrix, $\boldsymbol{I}$ is the state vector, $\boldsymbol{U}$ is the input vector, $\boldsymbol{Y}$ is the output vector and $\boldsymbol{C}$ is the output matrix. $\boldsymbol{B} = \frac{1}{\sigma L_r}\begin{bmatrix} 1 & 0 \\ 0 & 1 \end{bmatrix}$, $\boldsymbol{A} = \begin{bmatrix} -\frac{R_r}{\sigma L_r} & \omega_s \\ -\omega_s & -\frac{R_r}{\sigma L_r} \end{bmatrix}$, $\boldsymbol{C} = \begin{bmatrix} 1 & 0 \\ 0 & 1 \end{bmatrix}$, $\boldsymbol{I} = \begin{bmatrix} \widetilde{i}_{rd} \\ \widetilde{i}_{rq} \end{bmatrix}$ and $\boldsymbol{U} = \begin{bmatrix} u_{rd} - \frac{\omega_s L_m U_s}{\omega_1 L_s} \\ u_{rq} \end{bmatrix}$.

Equation (A1) can be decoupled with the state feedback method [28]:

(1) First, d_i (i = 1, 2) is calculated:

$$c_1\boldsymbol{A}^0\boldsymbol{B} = \begin{bmatrix} \frac{1}{\sigma L_r} & 0 \end{bmatrix} \tag{A3}$$

The minimum l value that makes $c_1A^lB \neq \mathbf{0}$ is 0, so $d_1 = 0$. In the same way, $d_2 = 0$ can be obtained.

(2) Then, we define the following matrix according to $d_{i:}$

$$\boldsymbol{D} = \begin{bmatrix} c_1\boldsymbol{A}^{d_1} \\ c_2\boldsymbol{A}^{d_2} \end{bmatrix} = \begin{bmatrix} c_1\boldsymbol{A}^{0} \\ c_2\boldsymbol{A}^{0} \end{bmatrix} = \begin{bmatrix} 1 & 0 \\ 0 & 1 \end{bmatrix} \tag{A4}$$

$$\boldsymbol{E} = \begin{bmatrix} c_1\boldsymbol{A}^{d_1}\boldsymbol{B} \\ c_2\boldsymbol{A}^{d_2}\boldsymbol{B} \end{bmatrix} = \begin{bmatrix} \frac{1}{\sigma L_r} & 0 \\ 0 & \frac{1}{\sigma L_r} \end{bmatrix} \tag{A5}$$

$$\boldsymbol{L} = \boldsymbol{DA} = \begin{bmatrix} -R_r/(\sigma L_r) & \omega_s \\ -\omega_s & -R_r/(\sigma L_r) \end{bmatrix} \tag{A6}$$

Since the matrix $\boldsymbol{E}$ is a non-singular matrix, the above equation of state can be decoupled.

(3) Finally, we decouple the equation of state

$$\dot{\boldsymbol{X}} = (\boldsymbol{A} + \boldsymbol{BK})\boldsymbol{X} + \boldsymbol{BFU} = \sigma L_r \begin{bmatrix} u_{rd} - \frac{\omega_s L_m U_s}{\omega_1 L_s} \\ u_{rq} \end{bmatrix} \tag{A7}$$

In the equation, the matrix $\boldsymbol{F}$ is the input transformation matrix, and $\boldsymbol{F} = \boldsymbol{E}^{-1}$; the matrix $\boldsymbol{K}$ is the state feedback matrix, and $\boldsymbol{K} = -\boldsymbol{E}^{-1}\boldsymbol{L}$. The DFIG control model decoupling can be obtained from Equation (A7), as shown in Figure 20. The dashed box in Figure 20 is the target model that needs to be decoupled.

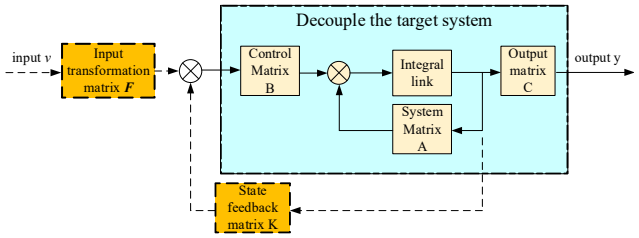

Figure A1. DFIG control model decoupling diagram.

Accordingly, Equation (A7) can be rewritten as:

$$\begin{cases} \dot{\tilde{i}}_{rd} = (\omega_r - \omega_1)\frac{\sigma L_r L_m U_s}{\omega_1 L_s} + \sigma L_r u^*_{rd} \\ \dot{\tilde{i}}_{rq} = \sigma L_r u^*_{rq} \\ \dot{\omega}_r = -\frac{n_p L_m U_s}{J\omega_1 L_s}\tilde{i}_{rd} - \frac{D}{J}\omega_r + \frac{T_L}{J} \end{cases} \tag{A8}$$

where u^*_{rd}, u^*_{rq} represent the input quantity of the control decoupling model.

As can be seen from Equation (A8), the state equation of the DFIG system changes from a third-order model to a model composed of a first-order and a second-order model after decoupling through state feedback. In the case of S29SO, based on the decoupling model, the control ratios u^*_{rd} and u^*_{rq} of the rotor current were designed with the back-stepping control method.

References

1. Chen, G.; Li, M.; Xu, T.; Liu, M. Study on technical bottleneck of new energy development. *Proc. CSEE* **2017**, *37*, 20–26.
2. Deng, W.; Wang, H.; Chang, X.; Guo, X. Cause analysis on subsynchronous oscillation in large-scale doubly-fed wind farm. *High. Volt. Appar.* **2019**, *55*, 215–221.
3. Liu, R.; Yao, J.; Wang, X.; Sun, P.; Pei, J.; Hu, J. Dynamic stability analysis and improved LVRT schemes of DFIG-based wind turbines during a symmetrical fault in a weak grid. *IEEE Trans. Power Electron.* **2020**, *35*, 303–318. [CrossRef]
4. Jiang, Q.; Wang, L.; Xie, X. Study on oscillations of powerelectronized power system and their mitigation schemes. *High. Volt. Eng.* **2017**, *43*, 1057–1066.

5. Xue, A.; Fu, X.; Qiao, D.; Wang, Y.; Wang, J. Review and prospect of research on sub-synchronous oscillation mechanism for power system with wind power participation. *Electr. Power Autom. Equip.* **2020**, *40*, 118–128.
6. Li, H.; Abdeen, M.; Chai, Z.; Kamel, S.; Xie, X.; Hu, H.; Wang, K. An improved fast detection method on subsynchronous resonance in a wind power system with a series compensated transmission line. *IEEE Access* **2019**, *6*, 61512–61522. [CrossRef]
7. Xie, X.; Wang, L.; He, J.; Liu, H.; Wang, C.; Zhan, Y. Analysis of subsynchronous resonance/oscillation types in power systems. *Power Syst. Technol.* **2017**, *41*, 1043–1049.
8. Liu, H.; Xie, X.; Zhang, C.; Li, Y.; Liu, H.; Hu, Y. Quantitative SSR analysis of series-compensated DFIG-based wind farms using aggregated RLC circuit model. *IEEE Trans. Power Syst.* **2017**, *32*, 474–483. [CrossRef]
9. Dong, X.; Tian, X.; Zhang, Y.; Song, J. Practical SSR incidence and influencing factor analysis of DFIG-based series-compensated transmission system in guyuan farms. *High Voltage Eng.* **2017**, *41*, 461–474.
10. Dong, H.; Su, M.; Liu, K.; Zou, W. Mitigation strategy of subsynchronous oscillation based on fractional-order sliding mode control for VSC-MTDC systems with DFIG-based wind farm access. *IEEE Access* **2020**, *8*, 209242–209250. [CrossRef]
11. Shair, J.; Xie, X.; Yang, J.; Li, J.; Li, H. Adaptive damping control of subsynchronous oscillation in DFIG-based wind farms connected to series-compensated network. *IEEE Trans. Power Deliv.* **2022**, *37*, 1036–1049. [CrossRef]
12. Shair, J.; Xie, X.; Li, Y.; Terzija, V. Hardware-in-the-Loop and field validation of a rotor-side subsynchronous damping controller for a series compensated DFIG system. *IEEE Trans. Power Deliv.* **2021**, *36*, 698–709. [CrossRef]
13. Leon, A.E.; Amodeo, S.J.; Mauricio, J.M. Enhanced compensation filter to mitigate subsynchronous oscillations in series-compensated DFIG-based wind farms. *IEEE Trans. Power Deliv.* **2021**, *36*, 3805–3814. [CrossRef]
14. Zhang, T.; Hao, Z.; Shu, J.; Zhao, Y.; Yuan, S. Research on SSO suppression of DFIG-based wind farm by impedance scanning. In Proceedings of the 2020 IEEE Power & Energy Society General Meeting (PESGM), Montreal, QC, Canada, 2–6 August 2020.
15. Meng, F.; Sun, D.; Zhou, K.; Wu, J.; Zhao, F.; Sun, L. A sub-synchronous oscillation suppression strategy for doubly fed wind power generation system. *IEEE Access.* **2021**, *9*, 83482–83498. [CrossRef]
16. He, Y.; Hu, J.; Xu, L. *The Operation Control of Grid-Connected Asynchronous Doubly-Fed Wind Turbine*, 1st ed.; China Electric Power Press: Beijing, China, 2012; pp. 21–23.
17. Zhao, X.; Peng, Z.; Tan, H.; Mao, Y.; Li, D. Sub-synchronous torsional interaction analysis of doubly-fed wind generator. *Electric. Power Sci. Eng.* **2018**, *34*, 12–17.
18. Chen, P.; Qi, C.; Chen, X.; Chen, J.; Li, C. Frequency response modeling and parameter identification of doubly-Fed wind farm with additional frequency control. *Trans. China Electrotech. Soc.* **2021**, *36*, 3293–3307.
19. Li, H.; Zhu, C.; Fan, Z.; Tan, Z.; Song, C. Research on maximum power point tracking strategy of wind turbine based second order sliding model-PID control. *Acta Energ. Sol. Sin.* **2022**, *43*, 306–314.
20. Xiong, P.; Sun, D.; Tan, H.; Mao, Y.; Li, D. Backstepping-based DPC strategy of a wind turbine-driven DFIG under normal and harmonic grid voltage. *IEEE Trans. Power Electron.* **2016**, *31*, 4216–4225. [CrossRef]
21. Ding, Y.; Kang, E.; Wang, S.; Chen, G.; Liu, F. Disturbance suppression for PMSM by a non-linear composite controller based on two-channel strategy. *IET-EPA* **2020**, *14*, 31–40. [CrossRef]
22. Yang, J.; Cai, H.; Zou, Z.; Xu, W.; Wu, J. Chaotic motion analysis and decoupling adaptive backstepping control of doubly-fed wind power system. *Acta Energ. Sol. Sin.* **2019**, *40*, 3605–3612.
23. Xia, W.; Wang, K.; Zhang, J.; Liu, D. Torque ripple suppression of permanent magnet synchronous motor with harmonic shaped rotors based on resonance controllers. *Proc. CSEE* **2019**, *39*, 5499–5508.
24. Chen, J.; Diao, L.; Du, H.; Fu, Y.; Liu, Z. Research of auxiliary inverter control strategy based on new resonant controller. *Trans. China Electrotech. Soc.* **2013**, *28*, 107–119.
25. Song, Y.; Nian, H. Integrated control strategy of DFIG based on vector resonant control under distorted grid voltage conditions. *Trans. China Electrotech. Soc.* **2014**, *29*, 187–199.
26. Yang, D.; Peng, Z.; Liu, J.; Shao, D.; Wu, N. D-q current decoupling for single-phase grid-connected converter based on non-delay. *Power. Syst. Technol.* **2022**, *46*, 1585–1594.
27. Xia, C.; Rahman, S.U.; Liu, Y. Analysis and design of current regulator stability during high-speed operation of permanent magnetic synchronous motor. *Proc. CSEE* **2020**, *40*, 303–312.
28. Chen, L.; Zhu, C.; Wang, Z.; Mao, Y.; Li, D. Decoupling control for active magnetic bearing high-speed flywheel rotor based on mode separation and state feedback. *Proc. CSEE* **2017**, *37*, 5461–5472.